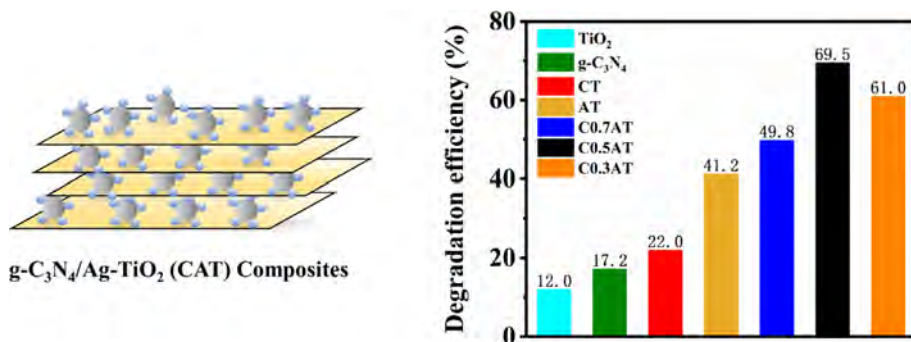Regular Article

Improved photocatalytic oxidation performance of gaseous acetaldehyde by ternary g-C$_3$N$_4$/Ag-TiO$_2$ composites under visible light

Congyu Wang [a,b], Zepeng Rao [a,b], Asad Mahmood [a], Xiao Wang [a], Yan Wang [a,*], Xiaofeng Xie [a], Jing Sun [a,*]

[a] State Key Lab of High Performance Ceramics and Superfine Microstructure, Shanghai Institute of Ceramics, Chinese Academy of Sciences, 1295 Dingxi Road, Shanghai 200050, China
[b] University of Chinese Academy of Sciences, 19 (A) Yuquan Road, Beijing 100049, China

GRAPHICAL ABSTRACT

g-C$_3$N$_4$/Ag-TiO$_2$ (CAT) Composites

ARTICLE INFO

ABSTRACT

In the process of photocatalytic oxidation (PCO), titanium dioxide (TiO$_2$) shows excellent capabilities. However, when TiO$_2$ is used to remove volatile organic compounds (VOCs), there are some drawbacks including weak adsorption of gaseous contaminants, insufficient utilization of sunlight, and rapid recombination of photogenerated carriers. Herein, a TiO$_2$-based ternary heterogeneous photocatalyst, g-C$_3$N$_4$/Ag-TiO$_2$, was successfully fabricated to photodegrade gaseous acetaldehyde (one of the representatives of oxygenated VOCs) under visible light. Among the various samples, the g-C$_3$N$_4$/50 wt% Ag-TiO$_2$ exhibited an excellent photocatalytic activity, which was 5.8 times of bare TiO$_2$. The mineralization efficiency of acetaldehyde was also increased by 3.7 times compared to bare TiO$_2$. The substantial improvement in the PCO performance of the ternary system can be associated with the good adsorption to acetaldehyde gas and light-harvesting capability, as well as improved charge separation process. The application of Langmuir-Hinshelwood kinetic model suggested that relative humidity played a significant role in the VOCs degradation. Also, the photodegradation of gaseous acetaldehyde primarily occurred on the catalysts surface. Based on several characterizations, i.e., UV–vis spectroscopy, photoluminescence spectrum, photocurrent spectroscopy and electron spin-resonance test, a suitable degradation mechanism is proposed. This study provides a novel ternary photocatalyst with improved photocatalytic performance and stability, which can be used for the low-concentration VOCs abatement in the indoor environment.

© 2021 Elsevier Inc. All rights reserved.

* Corresponding authors.
E-mail addresses: wangyan@mail.sic.ac.cn (Y. Wang), jingsun@mail.sic.ac.cn (J. Sun).

1. Introduction

With the rapid development of industrialization and the continuous consumption of energy, numerous environmental problems have become increasingly prominent [1]. Generally, the low boiling point organic pollutants, referred to as volatile organic compounds (VOCs), are responsible for indoor and outdoor air pollution. These VOCs can directly affect the human health as well as facilitate the formation of $PM_{2.5}$, O_3 and other secondary pollutants via a series of atmospheric reactions [2]. Although several technologies, e.g., adsorption and thermal decomposition, have been considered for the removal of VOCs, the photocatalytic oxidation (PCO) technology is regarded as a promising approach to address this longstanding issue of VOCs pollution by taking the advantages of PCO such as mild operating conditions (i.e., ambient temperature and atmospheric pressure), low energy consumption, high degradation efficiency for multiple contaminants, and easy operation [3,4]. Among the various oxide-based semiconductor materials, titanium dioxide (TiO_2) photocatalyst is one of the most studied materials for the photocatalytic applications due to its good oxidizing properties, resistance to photo-corrosion, and availability [5,6]. However, several disadvantages of TiO_2 still hinder its application in the VOCs abatement technology. For example, the inadequate adsorption capacity to dynamic gaseous pollutants leads to low degradation efficiency, which could be associated with the lower specific surface area [7,8]. Moreover, TiO_2, a wide bandgap semiconductor, can only absorb UV (ultraviolet) light ($\lambda < 390$ nm), which results in low utilization of sunlight [9,10]. The fast recombination of the photogenerated carriers in TiO_2 further limits its usefulness for the surface catalyzed reactions [11,12]. To overcome these issues, some attempts have been reported to modify the structure and composition of TiO_2, such as the control of crystal phase structure and defects [13], adjustment of energy band position [14], reduction of grain size [15], element doping [16], deposition of metallic cocatalysts [17], photosensitization of TiO_2 surface [18], formation of heterojunctions through compositing with other materials [19] and preparation of mesoporous structure [20], etc.

Recently, immense interest has been shown in the photocatalysis under visible light (encompass 45% of the solar spectrum) irradiation. For this purpose, graphite carbon nitride (g-C_3N_4) is the focus of interest for visible-light-induced water splitting applications [21], N_2 reduction [22] and contaminants degradation [23] reactions due to its excellent thermal and chemical stability and moderate bandgap. Additionally, g-C_3N_4 exhibits a graphene-like structure, which can be used as a composite material with other photocatalysts [24]. For example, it can be efficiently coupled with TiO_2 by forming a thin layer on TiO_2 surface. In this way, a larger specific surface area can be achieved, which will undoubtedly improve the overall absorptivity of the pollutants [25]. Moreover, it has been observed that by compositing TiO_2 and g-C_3N_4 might result in a photocatalyst framework, which is capable of light harvesting within the visible region of the solar spectrum [26]. Also, the formed heterojunction can improve the photogenerated charge separation process. For example, Sheng et al. [27] synthesized a three-dimensional g-C_3N_4/TiO_2 composite that exhibited effective PCO performance for methylene blue and phenol. The enhancement was mainly attributed to the three-dimensional structure, which improved the adsorption property and provided multidimensional channels for the hole-electron (e$^-$-h$^+$) pairs transmission. Similarly, Li et al. [28] prepared a g-C_3N_4-TiO_2 composite through heating g-C_3N_4 and nanotube titanic acid (NTA), and proved that this photocatalyst could degrade propylene efficiently under visible light irradiation. Li et al. [29] synthesized a hollow-sphere nano-heterojunction of g-C_3N_4@TiO_2 catalyst by annealing melamine and hollow sphere precursors. Its photocatalytic

performance for hydrogen generation was 5 times greater than g-C_3N_4@TiO_2 catalyst.

The role of metallic cocatalysts in photocatalytic reactions has been recognized recently. Precious metals such as Au, Ag, Pt, Pd, etc. can significantly boost photocatalytic activity of TiO_2 material. Firstly, due to the surface plasmon resonance (SPR) effect, the deposition of precious metals on the TiO_2 surface can improve the absorption and utilization of visible light [30]. Additionally, the contact between TiO_2 and precious metals will form a Schottky barrier at the interface. Then, the electrons on the conduction band (CB) of TiO_2 will migrate to metal cocatalysts due to the higher Fermi level of TiO_2 [31]. The photogenerated electrons are enriched on the metal clusters, and the photoinduced holes are transferred to TiO_2. Both of which cause the effective separation of photogenerated carriers. Eventually, these improvements enhance the photocatalytic performance [32]. Klein et al. [33] deposited mono- and bimetallic clusters on TiO_2 surface by γ-rays radiation, and investigated the effects of deposition methods on the PCO performance. Weon et al. [17] prepared platinum/titania and fluorine-titania/platinum catalysts for the PCO of toluene. These studies showed that metallic cocatalysts on TiO_2 surface can improve the photocatalytic activity for the gas-solid heterogeneous catalysis.

Considering the above, a ternary photocatalyst framework, g-C_3N_4/Ag-TiO_2, was prepared by a two-step method and studied its potential for the PCO of gaseous acetaldehyde under visible light irradiation. The deposition of Ag on the TiO_2 surface can broaden the optical absorption region owing to the SPR effect. The interface among the materials will further facilitate the charge separation. Moreover, compounding with two-dimensional semiconductor g-C_3N_4, which normally exhibits larger specific surface area, can improve the ability to adsorb gaseous pollutants and expand the response range of visible light. The formed heterostructure of photocatalysts further enhances the e$^-$-h$^+$ pairs separation, thereby facilitating the PCO performance. This work presents the development of a visible light active photocatalyst, which can be used for the VOCs removal under visible light irradiation.

2. Experimental

2.1. Chemicals

Degussa P25 (TiO_2) was bought from Evonik Industries AG, Germany. Melamine ($C_3H_6N_6$, AR, 99%), NaOH (AR, 96%) and $AgNO_3$ (AR, 99.8%) were obtained from Sinopharm Chemical Reagent CO., Ltd, China. 5,5-dimethyl-1-pyrroline N-oxide (DMPO, AR, 97%), p-benzoquinone (PBQ, AR, 99%), sodium borohydride ($NaBH_4$, AR, 98%) and 2,2,6,6-tetramethyl-1-piperidinyloxy (TEMPO, AR, 98%) were produced by the Aladdin Reagent Co., Ltd, China. All chemicals were used without further purification.

2.2. Preparation of samples

Graphitic carbon nitride (g-C_3N_4) was obtained by a direct high-temperature calcination method [34]. Typically, melamine (5 g) was calcined at 550 °C for 4 h with a heating rate of 10 °C/min. After naturally cooling down to ambient temperature, the obtained yellow lumps were ground in a mortar and pestle to achieve fine powder.

Ag-loaded TiO_2 (AT) was synthesized by a pH-adjusted chemical reduction procedure [35]. Initially, TiO_2 powder (120 mg) was dispersed in deionized water (100 mL). Then, 0.5 mL of 0.1 M NaOH solution was added dropwise to adjust the pH value of 8.5. Next, 0.56 mL of 0.2 M $AgNO_3$ solution was dripped into the mixture and stirred in the dark to achieve the adsorption equilibrium of Ag$^+$. The above suspension was transferred into a three-necked

flask connected to argon gas and continually stirred for 30 min. Next, 5.6 mL of 0.1 M NaBH$_4$ solution (0.1 M NaOH solution as solvent) was slowly added. After being stirred for 1 h, the mixture was centrifuged repeatedly and dried for 13 h to get AT sample with Ag content as 2 wt%. The final yield was 90.8%. The energy dispersive X-ray spectroscopy (EDS) mapping (Fig. S1) confirmed the elemental composition of AT sample. Previous studies [36,37] have proven that the composites prepared by loading 2% mass percentage of Ag nanoparticles on TiO$_2$ exhibit the optimal PCO efficiency during organic compounds degradation.

The g-C$_3$N$_4$/Ag-TiO$_2$ (CAT) composites were fabricated by mixing g-C$_3$N$_4$ and AT with different mass ratios: 30 mg/70 mg, 50 mg/50 mg, 70 mg/30 mg, and using 100 mL of deionized water. After ultrasonic treatment for 3 h, the as-prepared mixture was left to dry. The dried solid was calcined in air at 400 °C for 1 h to obtain CAT samples, designated as C0.7AT, C0.5AT, C0.3AT, respectively, and their yields were 96.4%, 97.1% and 96.9%, respectively. The g-C$_3$N$_4$/TiO$_2$ (CT) was synthesized with g-C$_3$N$_4$ and TiO$_2$ (1:1) by the same procedure, and the yield was 97.8%.

2.3. Characterization

The crystalline structure of the materials was performed on X-ray diffraction (XRD, D8 ADVANCE, Bruker, Germany). The Fourier transform infrared (FTIR) spectra were collected on the Thermofisher iN10 iZ10 spectrophotometer (ThermoFisher Scientific, USA), using the KBr pellet method. The morphology, microstructure and element analysis of samples were conducted by the transmission electron microscope (TEM, JEM-2100F, JEOL, Japan) coupled with an EDS detector. Microlab 310F Scanning Auger Microprobe spectrometer (Thermo VG Scientific Ltd, USA) was used to analyze the X-ray photoelectron spectroscopy (XPS). *In-situ* diffuse reflectance infrared Fourier transform spectroscopy (DRIFTS, IRTracer-100, Shimadzu Co., Ltd, China) was used to analyze the intermediate formation adsorbed on the surface of photocatalysts. UV–vis diffuse reflectance spectroscopy (DRS) was measured on Lambda 950 instrument (300–800 nm, PerkinElmer, USA). The N$_2$ adsorption-desorption isotherms and Brunauer-Emmett-Teller specific surface area (S$_{BET}$) analysis were conducted by ASAP 3000 (Micromeritics, USA) equipped with a nitrogen adsorption device. Photoluminescence (PL) spectra were acquired on the LS-55 fluorescence spectrophotometer (PerkinElmer, USA) excited by an excitation wavelength of 320 nm. The photocurrent study was performed in an electrochemical workstation (CHI 660D, Chenhua Instrument Co., Ltd, China). The electron spin resonance (ESR) signals were obtained on JES-FA200 electron paramagnetic resonance spectrometer (JEOL, Japan). The sample preparation methods for FTIR, TEM, *in-situ* DRIFTS, UV–vis DRS, PL, BET measurements and the experimental details of the photocurrent spectroscopy, ESR, and scavenger experiments are provided in the Supporting Information.

2.4. Assessment of adsorption character and photocatalytic performance

The tests were performed at room temperature and ambient pressure with a continuous gas flow reactor (Fig. S2). The 400 W xenon lamp with an intensity of 50 mW/cm^2 was used as the irradiation source, and a 420 nm cut-off filter was placed in front of the light source to test the performance of photocatalyst under visible light (the emission spectrum and spectral energy distribution are shown in Fig. S3). The relative humidity (RH) of the feed stream was set to 45%-55% through a humidifier to simulate the atmospheric environment. The concentration of acetaldehyde gas was set to 25 ppm by mixing canned acetaldehyde standard gas (50 ppm) with air in a ratio of 1:1.The flow rate was set to 20 sccm

through a computer programmed control system. The concentration of acetaldehyde gas at outlet was monitored through an online gas chromatography (GC), and the concentration data was obtained every five minutes. The specific experimental method was as follows: 100 mg of powder was dispersed in ethanol (2 mL). After ball milling in a bottle for 8 h, the suspension was evenly coated on the glass substrate (15 cm × 7.5 cm × 3 mm) by the doctor blade coating method, and then dried at 80 °C. The thickness of the photocatalyst layer over the glass substrate is 14.3 μm (Fig. S4). Finally, the glass substrate was put in a cuboid reaction chamber (20 cm × 8 cm × 2 cm). The distance between the glass substrate and the light source was 20 cm. The residence time of acetaldehyde gas on the photocatalyst was 12 min (residence time = 20*8*2 cm^3/20 sccm*15 cm/20 cm = 12 min). After achieving the adsorption-desorption equilibrium of flowing acetaldehyde gas, the xenon lamp was switched on. Additionally, the C0.5AT composite was used to carry out the cyclic test. The same dynamic adsorption-desorption and photodegradation routine were adopted, whilst using the same sample repeatedly. The interval of each cycle was 3 days. The saturated adsorption capacity (AC, mol/g) of acetaldehyde gas was calculated by AC = C$_0$ × ρ$_A$ × d × ν × {[$\int_0^t$(1-C/C$_0$) dt] $_{catalyst}$ − $\int_0^t$(1-C/C$_0$) dt $_{blank}$]}/(M × m), and the photodegradation rate (PR) of acetaldehyde gas was estimated by PR = (C$_0$-C)/C$_0$ × 100%, where C$_0$ (ppm) and C (ppm) represent the original concentration and the detected interval concentration of acetaldehyde gas, respectively. ρ$_A$ (g/cm^3) is the air density and d is the relative vapor density of acetaldehyde. ν (sccm) depicts the flow rate of acetaldehyde gas. M (g/mol) is the molar mass of acetaldehyde and m (g) represents the mass of a photocatalyst. The mineralization efficiency (ME) of acetaldehyde gas was calculated by ME = Δ[CO$_2$]/(2 × C$_{in}$) × 100%, where Δ[CO$_2$] is the variation value of initial and final CO$_2$ concentrations, C$_{in}$ is the inlet concentration of gaseous acetaldehyde, and (2 × C$_{in}$) represents the theoretical amount of carbon dioxide produced after acetaldehyde (C$_2$H$_4$O) is completely degraded.

3. Results and discussion

3.1. Component and morphology of the as-prepared catalysts

Fig. 1a shows the XRD peak profile of the g-C$_3$N$_4$, TiO$_2$, AT and CxAT (x = 0.7, 0.5, 0.3) samples. The characteristic peaks located at 25.4° (101), 37.8° (004), 48.1° (200), 53.9° (105), 55.1° (211), 62.7° (204), 68.7° (116), 70.3° (220), and 75.1° (215) were assigned to anatase TiO$_2$. Furthermore, 2θ located at 27.4° (001), 36.1° (101), 41.3° (111) and 54.4° (211) confirmed the rutile TiO$_2$. Two typical diffraction peaks were ascribed to g-C$_3$N$_4$, of which one at 13.2° corresponded to the (100) lattice facet, whilst the peak at 27.5° could be attributed to the (002) lattice facet. The effective compositing of TiO$_2$ and g-C$_3$N$_4$ appeared in CxAT samples, which exhibited individual diffraction peaks for two materials. It was observed that increased g-C$_3$N$_4$ content could make the intensity of characteristic peak around 27.4° stronger and following with a small angular position shift. No extra peak for the Ag element was observed, since the content of Ag is extremely low. Fig. 1b shows the FTIR spectra of the composites. For bare TiO$_2$, the peaks in the IR range of 700 to 500 cm^{-1} were assigned to Ti-O and Ti-O-Ti vibration [38]. Furthermore, other signals at 1650 and 3400 cm^{-1} corresponded to –OH (or H$_2$O) attached to the surface [39]. For g-C$_3$N$_4$, several peaks were recorded in the range of 1200–1700 cm^{-1}, which can be associated with the C—N vibrations of the heterocyclic rings [40]. Besides, a characteristic peak at 810 cm^{-1} corresponded to the typical flexural vibration of the tri-s-triazine structure [41]. All the main char-
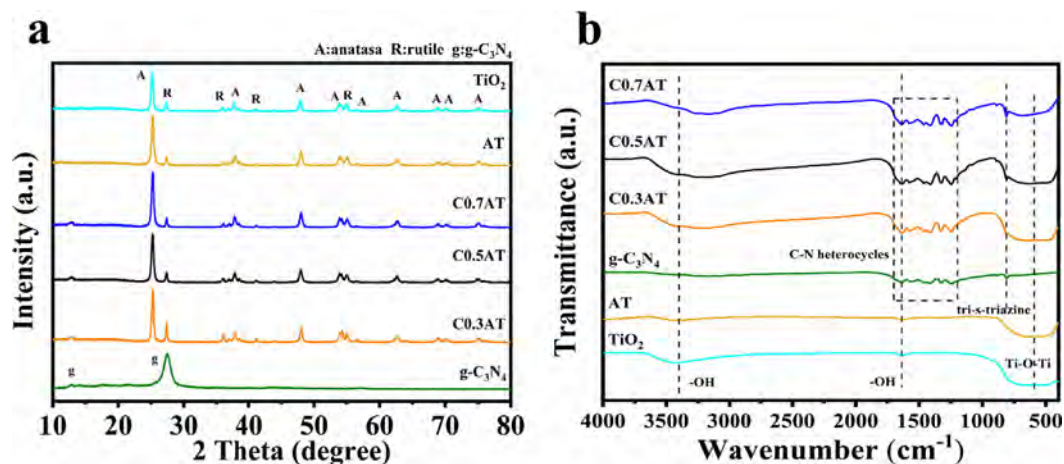
Fig. 1. (a) XRD peak profiles and (b) FTIR results of g-C$_3$N$_4$, TiO$_2$, AT and CxAT (x is the weight ratio of Ag-TiO$_2$ to g-C$_3$N$_4$, varied from 0.7, 0.5, 0.3) composites.

acteristic peaks exhibited in CxAT samples confirmed the coexistence of TiO$_2$ and g-C$_3$N$_4$.

The TEM characterization was used to study the microstructure of the composite structure in depth. The TEM analysis shows that the g-C$_3$N$_4$ prepared by high-temperature calcination and ultrasonic treatment had a two-dimensional lamellar structure (Fig. 2a). Fig. 2b shows somewhat spherical morphology of TiO$_2$ nanoparticles in the AT sample and their particle size ranged between 20 and 30 nm. Additionally, the existence of Ag nanoparticles could be traced on TiO$_2$. Fig. 2c shows that the AT nanoparticles were firmly attached to the sheet-like g-C$_3$N$_4$ in the C0.5AT composite. The presence of g-C$_3$N$_4$ reduced the agglomeration of TiO$_2$ nanoparticles and improved their dispersibility. This unique advantage enhanced the amount of exposed active sites, which is

undoubtedly useful for surface catalytic reactions. Fig. 2d is the HRTEM micrograph of the C0.5AT composite. The lattice fringe of 0.24 nm corresponds to (1 1 1) facet of Ag nanoparticles, while 0.35 nm was attributed to the (1 0 1) facet of anatase TiO$_2$ [30]. Besides, the EDS spectrum of C0.5AT composite was shown in Fig. S5. It can be inferred that the C and N elements shown in the spectrum were from g-C$_3$N$_4$, and the Ti and O elements might come from TiO$_2$. The mass percentages of elements in the results were in accordance with the calculated value.

The XPS spectra of C0.5AT composite were conducted to analyze the chemical elements and their states (Fig. 3). Five elements including Ti, O, C, N and Ag in C0.5AT composite were identified in the survey XPS spectrum (Fig. 3a). Moreover, the high-resolution spectral analysis of Ti 2p, O 1 s, C 1 s, N 1 s and Ag 3d
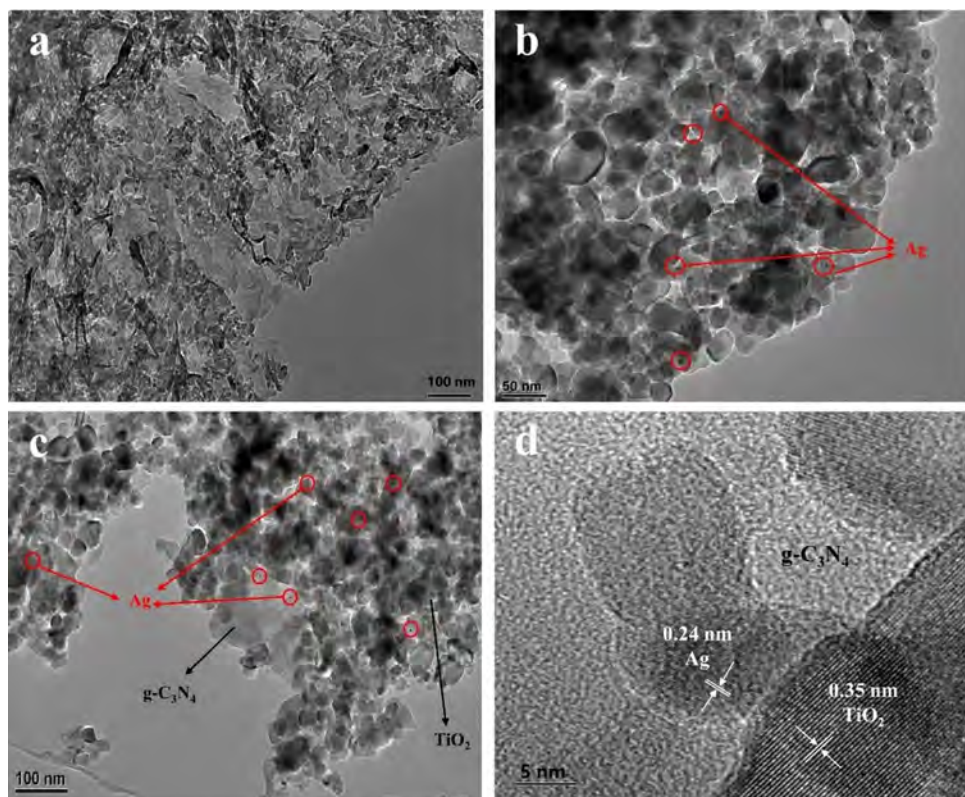

Fig. 2. TEM images of (a) g-C$_3$N$_4$, (b) AT, (c) C0.5AT composite; (d) HRTEM image of C0.5AT composite.
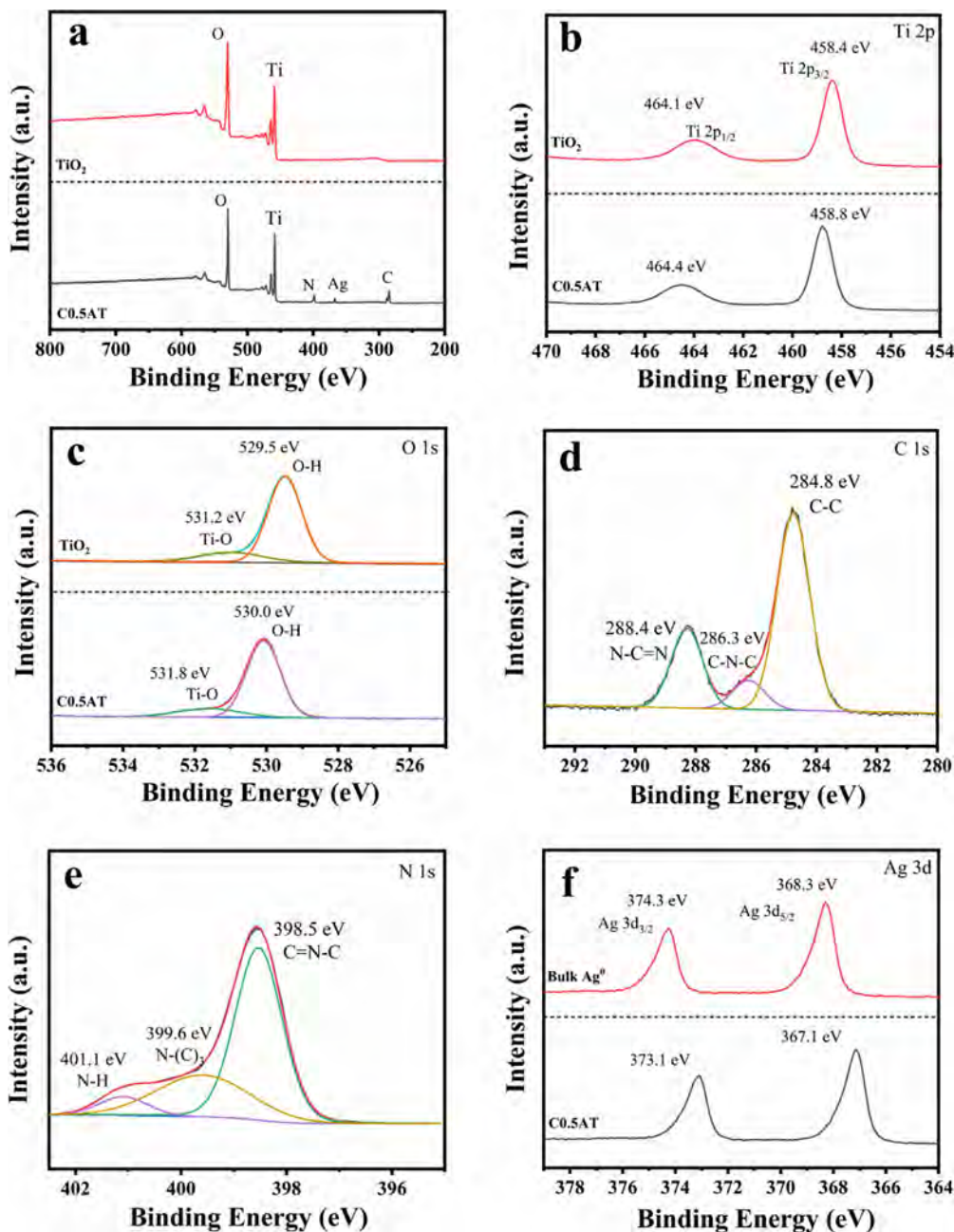
Fig. 3. XPS spectra of C0.5AT composite: (a) survey spectrum, (b) Ti 2p, (c) O 1 s, (d) C 1 s, (e) N 1 s and (f) Ag 3d. XPS spectra of pure TiO₂ and the high-resolution spectrum of Ag 3d in bulk Ag⁰ were provided.

were acquired (Fig. 3b-f). Two peaks at the binding energy (B.E) 464.4 eV (Ti $2p_{1/2}$) and 458.8 eV (Ti $2p_{3/2}$) in Ti 2p spectra (Fig. 3b), confirmed the existence of Ti^{4+} [42]. The O1s spectrum (Fig. 3c) was divided into two peaks corresponding to B.E 530.0 eV (O—H) and 531.8 eV (Ti-O) [43]. Three peaks at the B.E 288.4, 286.3 and 284.8 eV appeared in C1s curve (Fig. 3d), representing the N-C=N, C—N—C and C—C bonds [44]. The three peaks in N 1 s spectrum at the B.E 401.1 (N—H), 399.6 (N-$(C)_3$) and 398.5 eV (C=N-C) were detected (Fig. 3e) [27]. The characteristic Ag 3d peaks at the B.E 373.1 and 367.1 eV were observed (Fig. 3f), which were associated with Ag $3d_{3/2}$ (Ag⁰) and Ag $3d_{5/2}$ (Ag⁰) [45]. The split gap of Ag 3d doublet approximately 6 eV demonstrated that the Ag element existed as metallic Ag⁰ in the C0.5AT composite [46,47]. It is worth noting that due to the electron transfer between TiO₂ surface and metallic Ag, the binding

energies indicated by all peaks of Ti 2p and O 1 s in C0.5AT composite were higher than those of pure TiO₂ (Fig. 3b and c).Meanwhile, compared to bulk Ag⁰ (374.3 eV for Ag $3d_{3/2}$ and 368.3 eV for Ag $3d_{5/2}$) [48], the binding energies presented by the two Ag 3d peaks shifted to lower energies (Fig. 3f).

3.2. Adsorption character of the composites

The adsorption of target VOCs on the catalyst surface is an essential step during the gas-solid heterogeneous catalysis. It can be seen from the N₂ adsorption-desorption isotherms that all of the samples exhibited type IV curves (Fig. S6). By measuring and comparing the S_{BET} of bare TiO₂, g-C₃N₄ and CxAT (x = 0.7, 0.5, 0.3) composites (Table 1), it was observed that the S_{BET} of the TiO₂ (27.83 m²/g) has increased to a maximum value (78.88 m²/

Table 1
S_{BET} values of the investigated samples.

Samples	S_{BET} (m²/g)
TiO₂	27.83
g-C₃N₄	54.47
AT	30.24
C0.7AT	65.60
C0.5AT	71.62
C0.3AT	78.88

g) for the composites by incorporating g-C₃N₄. The ultrasonic treatment in the process of preparing CxAT composites lead to the formation of g-C₃N₄ nanosheets, resulting in the larger S_{BET} of CxAT composites than that of g-C₃N₄. After achieving the adsorption-desorption equilibrium of gaseous acetaldehyde on photocatalysts, the dynamic adsorption curve and saturated adsorption capacity of samples were obtained (Fig. 4). It took more than 120 min for CxAT composites to reach the saturated adsorption, which was a long time compared with the bare TiO₂ (100 min). The adsorption capacities for acetaldehyde gas of TiO₂ (0.029 mol/g), g-C₃N₄ (0.05 mol/g), AT (0.036 mol/g) and CxAT (0.125 mol/g, 0.152 mol/g and 0.177 mol/g) composites were calculated from the adsorption–desorption curves area. Consequently, it can be inferred that the existence of g-C₃N₄ substantially improved the adsorption capability of the composite structure.

3.3. Photocatalytic activity measurement

The prepared TiO₂, g-C₃N₄, CT, AT and CxAT (x = 0.7, 0.5, 0.3) composites were subjected to the photocatalytic degradation (160 min) for flowing acetaldehyde gas under visible light. A control experiment without any photocatalyst was performed and almost no degradation of acetaldehyde gas occurred (Fig. S7). The photocatalytic test results (Fig. 5b) showed that bare TiO₂ and g-C₃N₄ exhibited poor photodegradation efficiency in the visible region. For example, bare TiO₂ only showed 12% photodegradation while g-C₃N₄ displayed 17.2% photodegradation efficiency. The photodegradation efficiencies of TiO₂-based binary photocatalysts that combined with g-C₃N₄ (CT samples) and Ag (AT samples) increased to 22.0% and 41.2%, respectively. The degradation efficiency decreased a little with the increasing reaction time in the case of AT catalyst (Fig. 5a), which could be associated with partial deactivation of the catalyst due to the accumulation of the intermediates and carbonaceous residues on the catalyst surface. The

C0.5AT composite showed a tremendous increase in the photocatalytic performance contrasted to bare TiO₂. For example, the photodegradation efficiency of 69.5% was recorded under visible light irradiation, which is 5.8 times higher than bare TiO₂. It can be inferred that by depositing Ag and further compositing with g-C₃N₄, the photocatalytic activity of TiO₂ could be significantly improved. The corresponding reaction kinetics was investigated by establishing a model to determine the reaction rate constants of acetaldehyde removal. The specific formula is: $-\ln (C/C_0) = kt$, where k is the first-order reaction rate constant. As shown in Fig. 5(c), within the first 70 minutes of the reaction, the kinetic model curves presented a linear trend, indicating that the photocatalytic degradation of acetaldehyde gas fitted the pseudo-first-order kinetic model, and the calculated rate constants were 0.0018 min⁻¹, 0.0009 min⁻¹, 0.0040 min⁻¹, 0.0089 min⁻¹, 0.0074 min⁻¹, 0.0134 min⁻¹, 0.0099 min⁻¹ for TiO₂, g-C₃N₄, CT, AT and CxAT (x = 0.7, 0.5, 0.3) composites, respectively.

We also compared this work with other studies on TiO₂-based composites used for PCO of acetaldehyde gas (Table 2). In particular, it is evident that when the binary photocatalyst g-C₃N₄/TiO₂ was used to photodegrade 20 ppm of gaseous acetaldehyde under visible light, the photodegradation efficiency was only 18.4%, which is similar to our study in Fig. 5a, confirming the superiority of the ternary system. Even with larger specific surface area and using UV light irradiation, other photocatalysts could not achieve such an outstanding degradation efficiency of acetaldehyde. Overall, the CAT composites exhibited greater potential for sunlight harvesting and removal of gaseous acetaldehyde. The mineralization efficiency can be used to evaluate the complete degradation degree of acetaldehyde by a photocatalyst. It can be seen in Fig. 5d that 6.1 ppm carbon dioxide was released while the mineralization efficiency was only at 12.2% when TiO₂ was used as the photocatalyst. With the promotion of degradation efficiency, the mineralization efficiency of C0.5AT composite reached the highest at 57.7%, which increased 3.7 times compared with bare TiO₂. Additionally, the results of in-situ DRIFTS in Fig. S8 and Table S1 were used to study the intermediate products of C0.5AT composite in visible-light photodegradation of gaseous acetaldehyde. These results were the same as the existing reports [49,50].

To evaluate the durability of composite, PCO of acetaldehyde gas with prolonged reaction time and cyclic tests by C0.5AT composite were performed under the same experimental conditions (Fig. S9). The photocatalyst still maintained excellent photocatalytic performance under continuous irradiation for 600 min or after four cycles. Furthermore, the high-resolution spectrum of
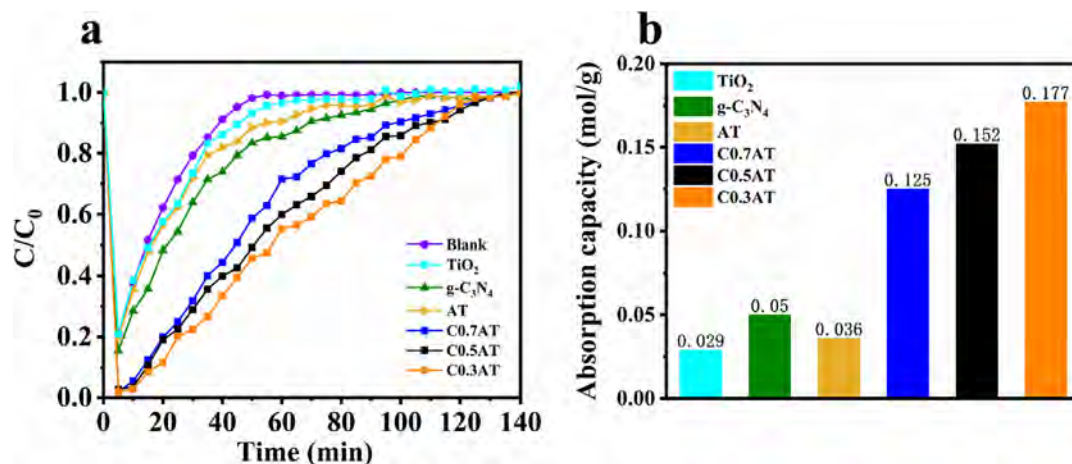

Fig. 4. (a) Dynamic adsorption experiments and (b) The saturated adsorption capacity for gaseous acetaldehyde (concentration of 25 ppm, flow rate of 20 sccm) in 140 min by TiO₂, g-C₃N₄, AT and CxAT (x = 0.7, 0.5, 0.3) composites (Repeat experiments for 3 times).
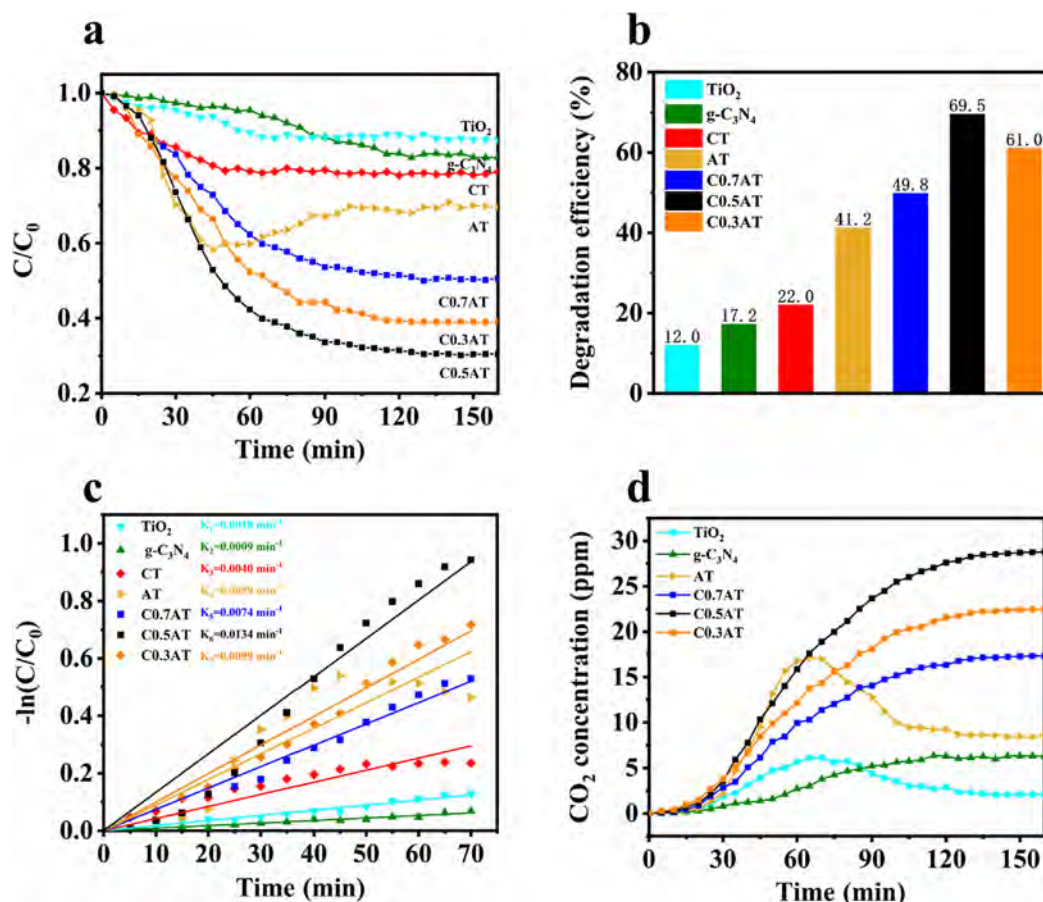
Fig. 5. (a) Photodegradation test for flowing acetaldehyde gas (concentration of 25 ppm, flow velocity of 20 sccm); (b) Stoichiometric diagram of degradation efficiency; (c) Corresponding pseudo-first-order kinetic models and (d) CO_2 generation curves after photodegradation of acetaldehyde on TiO_2, g-C_3N_4, AT and CxAT (x = 0.7, 0.5, 0.3) composites under 400 W xenon lamp with 420 nm cut-off filter (Repeat experiments for 3 times).

Table 2
Comparison of different photocatalysts in PCO of gaseous acetaldehyde.

Photocatalyst	S_{BET} (m^2/g)	Reaction system	Degradation efficiency	Reference
g-C_3N_4/Ag-TiO_2	71.62	Photocatalyst: 0.1 g; Gas: 25 ppm; Dynamic (20 mL/min); Visible light; Time: 160 min	69.5%	This work
g-C_3N_4/TiO_2	59.01	Photocatalyst: 20 cm^2; Gas: 20 ppm; Dynamic (50 mL/min); Visible light; Time: 30 min	18.4%	[51]
Cu/WO_3@Cu/N-TiO_2	93.6	Photocatalyst: 0.1 g; Gas: 610 ppm; Static; Visible light; Time: 24 h	≈66%	[52]
Fe-TiO_2	13.30	Photocatalyst: 0.17 g; Gas: 95 ppm; Dynamic (7 L/min); Visible light; Time: 1050 min	65%	[53]
N-TiO_2@aTiO_2	142.40	Photocatalyst: 0.1 g; Gas: 500 ppm; Dynamic (10 mL/min); Visible light; Time: 360 min	25%	[16]
TiO_2-UiO-66-NH_2	280.56	Photocatalyst: 0.1 g; Gas: 30 ppm; Dynamic (100 mL/min); UV light; Time: 720 min	70.74%	[54]
MT@rGO	16.80	Photocatalyst: 0.1 g; Gas: 500 ppm; Dynamic (8 mL/min); UV–visible light; Time: 150 min	70%	[7]
rGO-TiO_2	227.30	Photocatalyst: 0.1 g; Gas: 25 ppm; Dynamic (80 mL/min); UV light; Time: 160 min	42%	[8]

Ag 3d in C0.5AT composite after the reaction was determined by XPS (Fig. S10). It can be seen that the valence state of Ag element remained unchanged after photocatalytic degradation reaction. These results demonstrated that C0.5AT composite could be used as potential photocatalyst in the photocatalytic reactor for the low-concentration VOCs removal under visible light.

3.4. Kinetic study

To elucidate the degradation mechanism of acetaldehyde gas, we performed the kinetic study using the Langmuir-Hinshelwood (L-H) kinetic models [55,56]. Three samples, i.e., pure TiO_2, g-C_3N_4 and C0.5AT were selected for the kinetic study. The experimental PCO rate (r, ppm min^{-1}) of gaseous acetaldehyde can be calculated from the mass balance for a plug flow reactor, given

by $-r$ = v/V × [(C_0-C)/C_0], where v (20 sccm) is the flow rate of the feeding gas, V (320 mL) is the volume of the reaction chamber, and C_0 (ppmv) and C (ppmv) are the initial and outlet concentration of acetaldehyde gas, respectively. As the glass-plate reactor model was used in the experiment, it is assumed that the mass transfer is not the limiting step and the effect of intermediate is neglected. In this case, velocity profile is considered uniform and the dispersion (Dax/uL ≈ 0) is considered negligible.

Seven L-H kinetic models were used, which are based on several assumptions given in Table 3. These models can be used to comprehend the role of water and VOCs in a gas-phase photodegradation reaction and whether a reaction occurs on a catalyst surface or in the gas phase. Additionally, the adsorption equilibrium constants of water and VOCs can be used to determine their relative affinity towards a catalyst surface. A non-linear least square

Table 3
The kinetic models and rate expressions applied to experiments with/without H_2O [57].

Model	Kinetic rate expression	Assumption
1	$-r = k \times \frac{K_{AC}C_{AC}}{1+K_{AC}C_{AC}}$	Reaction of gaseous acetaldehyde adsorbed on catalyst surface but H_2O does not participate in the reaction.
2	$-r = k \times \frac{K_{AC}C_{AC}K_{H2O}C_{H2O}}{1+K_{AC}C_{AC}}$	Reaction of gaseous acetaldehyde adsorbed on catalyst surface and react with H_2O.
3	$-r = k \times \frac{K_{AC}C_{AC}}{(1-K_{AC}C_{AC}+K_{H2O}C_{H2O})}$	Gaseous acetaldehyde and water adsorbed on catalyst surface but H_2O does not take part in the reaction.
4	$-r = k \times \frac{K_{AC}C_{AC}K_{H2O}C_{H2O}}{(1+K_{AC}C_{AC}+K_{H2O}C_{H2O})}$	Reaction of gaseous acetaldehyde and H_2O adsorbed on catalyst surface.
5	$-r = k \times \frac{K_{AC}C_{AC}}{(1+K_{AC}C_{AC})} + \frac{K_{H2O}C_{H2O}}{(1+K_{H2O}C_{H2O})}$	Reaction of gaseous acetaldehyde and H_2O adsorbed on different active sites.
6	$-r = k \times \frac{K_{AC}C_{AC}K_{H2O}C_{H2O}}{(1+K_{H2O}C_{H2O})}$	Reaction of H_2O adsorbed on catalyst surface and gaseous acetaldehyde.
7	$-r = k \times \frac{(K_{AC}C_{AC}K_{H2O}C_{H2O})^{1/2}}{[1+(K_{AC}C_{AC})^{1/2}+(K_{H2O}C_{H2O})^{1/2}]^2}$	Reaction of gaseous acetaldehyde and H_2O dissociatively adsorbed on catalyst surface.

regression analysis was used to evaluate the goodness of fit and to determine the kinetic parameters, which includes the rate constant (k, $ppmv$ min^{-1}), the adsorption equilibrium constant of gaseous acetaldehyde (K_{AC}, $ppmv^{-1}$) and the adsorption equilibrium constant of H_2O (K_{H2O}, $ppmv^{-1}$). The accuracy of a model can be determined by evaluating values of the residual sum of squares (RSS) and the squared correlation coefficient (R^2). The smaller value of RSS or the larger value of R^2 depicts better reliability of a model.

Table 4 shows various kinetic parameters, RSS and R^2 determined through the L-H models for selected samples. Model 6, which assumes that the degradation reaction occurred in the gas phase, did not fit the experimental data (no rational parameters could be determined), indicating that the PCO of gaseous acetaldehyde mostly occurred on the photocatalyst's surface. By comparing the values of RSS and R^2, it can be concluded that for TiO$_2$ and C0.5AT, Model 7 is the most suitable kinetic model, which assumes that the acetaldehyde and water molecules dissociated and adsorbed on the photocatalyst's surface, and further participated

in the reaction. For g-C$_3$N$_4$, Model 3 gives a high R^2 value. The results further predicted that the corresponding K_{AC} values are greater than K_{H2O} values, indicating that acetaldehyde molecules were more easily adsorbed on the photocatalyst's surface than H_2O molecules. It has been widely explored that an optimum relative humidity (RH) value is important for excellent PCO performance. For example, Chevalier et al. [58] studied the adsorption of VOCs (acetone, o-xylene, and toluene) on HKUST-1 metal-organic framework (MOF) under different RH (0, 20, and 40%) values. The results showed 43% and 97% decrease in the absorptivity corresponding to 20% and 40% RH values, respectively. Therefore, appropriate RH is crucial during the PCO reaction. If the RH value is higher than a certain amount, the PCO performance will significantly decrease [59]. This behavior can be explained as follows: because of the competitive adsorption between the H_2O and VOC molecules, some of the H_2O molecules may occupy the active sites on the surface [60]. In addition, high RH can result in the formation of water film formed by H_2O molecules on the catalyst surface, which will consequently obstruct the physical interaction between VOCs and photocatalyst [61]. Thus, higher K_{AC} values contrasted to K_{H2O} values suggested that acetaldehyde strongly interacted with the catalyst surface and therefore efficiently degraded. Moreover, if we compare the k values of TiO$_2$ and C0.5AT in model 7, it can be seen that C0.5AT exhibited a high k (1.1686 ppmv min^{-1}) value compared to bare TiO$_2$ (0.0166 ppmv min^{-1}). Thus, the degradation rate of gaseous acetaldehyde on C0.5AT is greater than that on TiO$_2$, which also has been evidenced from the photodegradation experiments results (Fig. 5a). Previously, Vittadini et al. [62] have carried out density functional theory (DFT) calculations and compared molecular and dissociative adsorption of water molecules on anatase TiO$_2$ (101) surface. The computational results showed that dissociative adsorption of water molecules on anatase TiO$_2$ (101) is more favorable compared to molecular adsorption. Thus, the fitting of Model 7 to our experimental results gives a good prediction as anticipated. We also tested the effect of relative humidity by increasing it from 45% to 55%, which demonstrated a significant decrease in the photodegradation efficiency under visible light irradiation (Fig. 6).

Through the comparative analysis of the experimental rate and predicted rate values (Fig. S11), it can be concluded that the experimental rates of TiO$_2$, C0.5AT composite (corresponding to Model 7) and g-C$_3$N$_4$ (corresponding to Model 3) fitted well with the predicted rates in the model, which verified the accuracy of the pro-

Table 4
Kinetic and adsorption equilibrium parameters based on experimental data and rate expression in the model; residual sum of squares (RSS) and squared correlation coefficient (R^2).

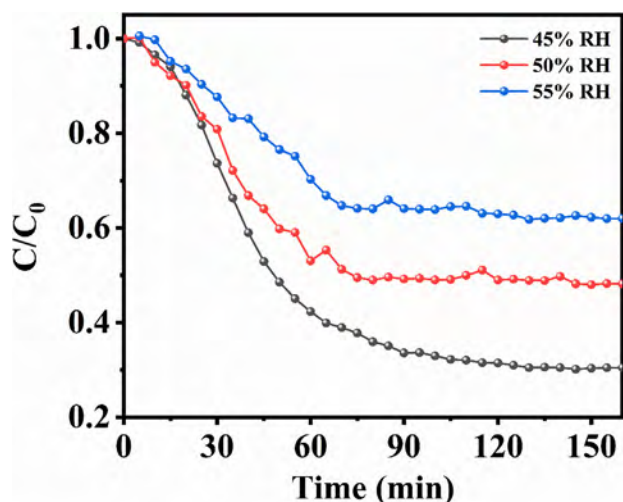|	L-H Kinetic Models						
	Model 1	Model 2	Model 3	Model 4	Model 5	Model 6	Model 7
TiO$_2$							
k ($ppmv$ min^{-1})	0.012	0.014	0.012	0.012	0.047	–	0.017
K_{AC} ($ppmv^{-1}$)	0.068	0.068	0.385	2.010	0.056	–	8.266
K_{H2O} ($ppmv^{-1}$)	–	8.80×10^{-5}	4.70×10^{-4}	3.30×10^{-6}	3.80×10^{-5}	–	3.59×10^{-2}
RSS	1.53×10^{-5}	1.52×10^{-5}	1.78×10^{-5}	1.78×10^{-6}	1.72×10^{-5}	–	1.51×10^{-5}
R^2	0.92	0.92	0.90	0.90	0.91	0.18	**0.93**
g-C$_3$N$_4$							
k ($ppmv$ min^{-1})	0.254	0.098	0.050	0.012	0.015	–	0.840
K_{AC} ($ppmv^{-1}$)	1.45×10^{-3}	5.70×10^{-4}	1.25×10^{-2}	2.010	0.235	–	0.017
K_{H2O} ($ppmv^{-1}$)	–	6.41×10^{-4}	5.00×10^{-5}	6.00×10^{-5}	1.25×10^{-4}	–	7.01×10^{-3}
RSS	2.00×10^{-5}	1.96×10^{-5}	2.92×10^{-5}	1.12×10^{-4}	2.27×10^{-4}	–	2.21×10^{-5}
R^2	0.96	0.96	**0.97**	0.903	0.70	0.08	0.96
C0.5AT							
k ($ppmv$ min^{-1})	0.078	0.035	0.083	0.083	0.071	–	1.169
K_{AC} ($ppmv^{-1}$)	0.048	0.048	0.082	1.968	0.037	–	0.039
K_{H2O} ($ppmv^{-1}$)	–	2.25×10^{-4}	7.76×10^{-5}	2.35×10^{-6}	4.62×10^{-4}	–	1.93×10^{-5}
RSS	4.80×10^{-4}	5.50×10^{-4}	$5.50 \times 10^{-}$	5.55×10^{-4}	5.55×10^{-4}	–	4.90×10^{-4}
R^2	0.94	0.94	0.93	0.93	0.93	0.14	**0.95**

Fig. 6. The PCO of gaseous acetaldehyde under visible light by C0.5AT composite in different humidifies (Repeat experiments for 3 times).

posed models. Based on the kinetic study, it can be anticipated that water dissociatively adsorbed on the catalyst's surface and actively converted to hydroxyl and oxide radicals, which then facilitated the photodegradation of gaseous acetaldehyde. Due to the stronger affinity of acetaldehyde molecules compared to water molecules, more mass transfer from the gas phase of acetaldehyde to the solid surface occurred, thus, the degradation reaction proceeded accordingly. The kinetic results determined some useful parameters which can be considered for the rational design of a photocatalytic reactor.

3.5. The mechanism of photocatalytic degradation

UV–vis DRS has been applied to measure the optical absorption characteristics and bandgap energy of the photocatalysts. Bare TiO_2 exhibited the characteristic absorption edge at 390 nm (Fig. 7a), which corresponds to its electronic transition of the bandgap. The main absorption edge of g-C_3N_4 appeared at 460 nm because of its narrow bandgap [63]. It is worth noting that when Ag and g-C_3N_4 were added, the absorption edges of CxAT composites all had a remarkable redshift to the higher wavelength, indicating the visible light absorption of composites was significantly enhanced. The bandgap energies (E_g) of the investigated materials were calculated by Kubelka-Munk function: $[F(R_\infty) \cdot h\upsilon]^{1/2} = A \cdot (h\upsilon - E_g)$, $F(R_\infty) = (1 - R_\infty)^2/2R_\infty$. where R_∞ is the limiting reflectance of infinite thickness sample, $F(R_\infty)$ is Kubelka-Munk function, $h\upsilon$ represents the light quantum and A is a constant [64]. The E_g values of TiO_2, g-C_3N_4, CT, AT and CxAT (x = 0.7, 0.5, 0.3) composites were calculated as 3.14, 2.60, 2.77, 2.95, 2.70, 2.62 and 2.48 eV, respectively (Fig. 7b). The calculated bandgap energies of CxAT composites are smaller in contrast to g-C_3N_4, TiO_2 and other binary compounds, which is mainly caused by the synergism between the ternary systems. The potentials of the conduction band (CB) and valence band (VB) for the samples were evaluated through equations (1) and (2) [65]:

$$P_{VB} = \gamma - P^e + 1/2E_g \qquad (1)$$

$$P_{CB} = P_{VB} - E_g \qquad (2)$$

where P_{CB} and P_{VB} depict the potentials of CB and VB, respectively, The γ values of TiO_2 and g-C_3N_4 are 5.81 and 4.64 eV, which represents the electronegativity of materials [66]. P^e depicts the constant value of free-electron energy. Therefore, according to

equations (1) and (2), it can be calculated that E_{VB} of g-C_3N_4 and TiO_2 are 1.44 eV and 2.88 eV, and their E_{CB} are −1.16 eV and −0.26 eV, respectively. Therefore, according to equation (1) and (2), the P_{VB} of TiO_2 and g-C_3N_4 are calculated to 2.88 and 1.44 eV, and the P_{CB} are −0.26 and −1.16 eV, respectively.

The separation and recombination of photoinduced charges in photocatalysts were studied by using the PL spectra (Fig. 8a, b). The recombination of photoinduced e^- and h^+ formed by light excitation can emit fluorescence, which can be recorded in the form of PL spectrum. Therefore, the lower PL intensity usually denotes the weaker recombination of photoinduced charges. Since the different emission bands between g-C_3N_4 and TiO_2 at an excitation wavelength of 320 nm, their PL intensities were compared with CT, AT and C0.5AT composites in a specific wavelength range. It was observed that the g-C_3N_4 band was intense near 460 nm, which matches its bandgap. In contrast to g-C_3N_4, the peak intensities of CT, AT and C0.5AT composites were much lower, indicating that these composites had weaker recombination of photoinduced charges. The PL intensity of C0.5AT composite was lower than that of TiO_2, CT and AT around the emission peak of 390 nm, which suggested that the separation of photogenerated carriers in C0.5AT composite was much improved.

The photocurrent spectroscopy (Fig. 8c) was used to research the generation and separation of photogenerated charges. Comparing with bare TiO_2, the photocurrent densities of the CxAT composites increased, indicating that the introduction of g-C_3N_4 and Ag increased the optical absorption and promoted the production and separation of photogenerated charges. Especially, the C0.5AT composite displayed the highest photocurrent density, indicating that it has a higher photogenerated carrier separation capability. However, excessive g-C_3N_4 might cover the reactive sites, which inhibited the migration of the photogenerated carriers, eventually resulting in a decrease in the photocurrent intensity. The PL and photocurrent studies confirmed that the ternary heterostructure promoted the separation of photoinduced charges efficiently.

ESR measurements (Fig. 9a and 9b) were used to survey the generation of active species ($\bullet O_2^-$ and $\bullet OH$) under visible light irradiation. The collected ESR signals of TiO_2, g-C_3N_4, AT and CxAT (x = 0.7, 0.5, 0.3) composites were categorizing as the typical patterns of DMPO- $\bullet O_2^-$ and DMPO- $\bullet OH$. The strongest signals of free radicals (including $\bullet OH$ and $\bullet O_2^-$ species) appeared for C0.5AT composite, which suggested that more radicles were formed. Moreover, it was observed that the intensities of $\bullet O_2^-$ species were higher than that of $\bullet OH$ species, suggesting that $\bullet O_2^-$ species dominated the PCO process in the ternary CxAT composites. To further determine the isolated role of $\bullet OH$ and $\bullet O_2^-$ during the photocatalytic reaction, scavenger experiments that used PBQ and TEMPO as $\bullet O_2^-$ quenching agent and $\bullet OH$ quenching agent were performed under the same condition of photodegradation test (Fig. 9c). After adding PBQ, the photodegradation efficiency for gaseous acetaldehyde decreased from 69.3% to 29.2%, demonstrating that $\bullet O_2^-$ species played a key role during the PCO reaction for gaseous acetaldehyde.

Based on the above results, two feasible photodegradation mechanisms for the gaseous acetaldehyde by the CAT composites under visible light can be proposed (Fig. 10). During the PCO reaction of acetaldehyde, the generation of photoinduced e^--h^+ pairs are anticipated in g-C_3N_4 by visible light excitation. The transformation of photoinduced e^- will occur from the CB of g-C_3N_4 to TiO_2 through Ag nanoparticles (Path 1). Possibly, photoinduced e^- can also migrate from the CB of g-C_3N_4 to TiO_2 through the heterojunction formed by the contact between g-C_3N_4 and TiO_2 (Path 2). Due to the CB of TiO_2 is higher than the Fermi level of Ag [67], e^- located on the CB of TiO_2 might transfer to Ag nanoparticles. All of these behaviors will impede the recombination process of photoinduced charges. Some of the separated electrons will combine
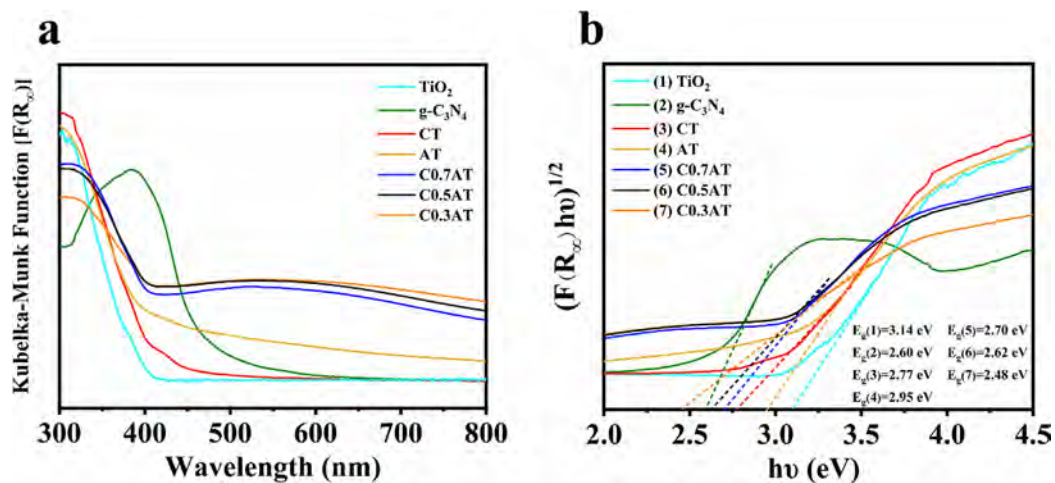
Fig. 7. (a) UV–vis diffuse reflectance spectroscopy (DRS) of as-prepared samples and (b) the corresponding Tauc plots representing $(F(R_\infty) h\upsilon)^{1/2}$ versus E_g.
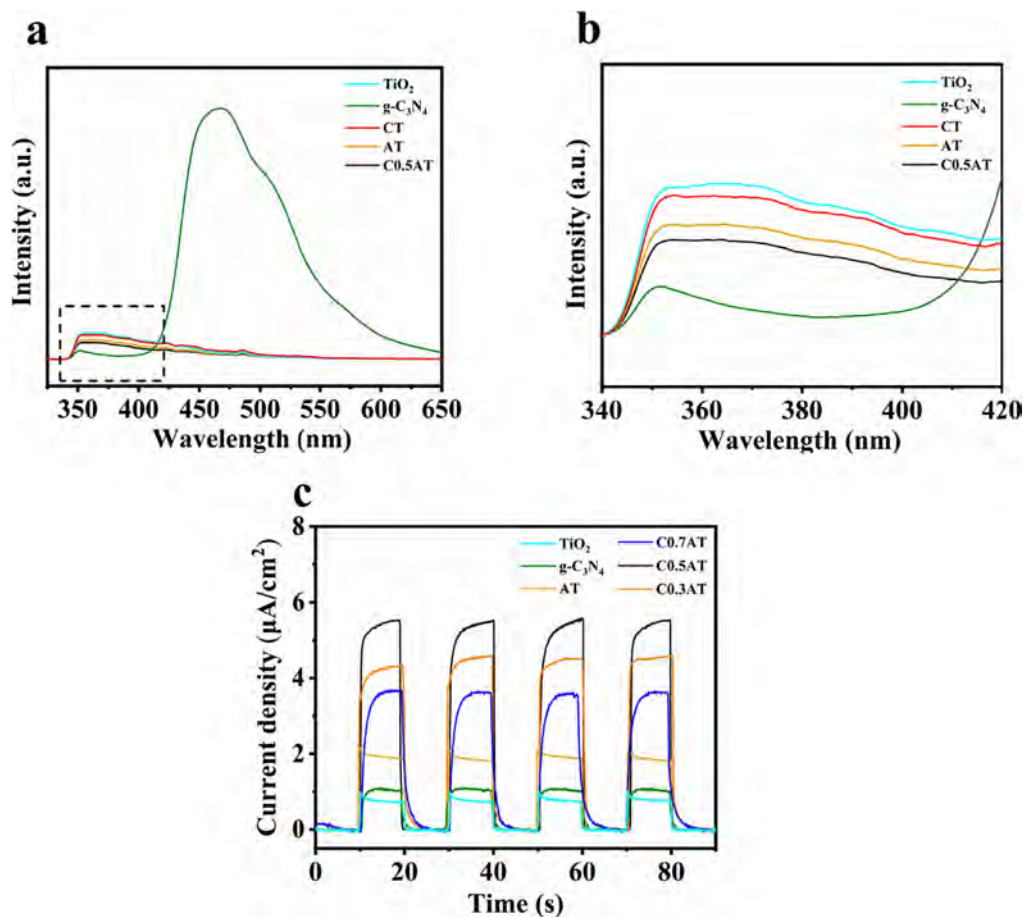

Fig. 8. (a) PL plots for g-C_3N_4, TiO_2, CT, AT and C0.5AT; (b) the magnified spectra of square frame; (c) photocurrent spectroscopies of TiO_2, g-C_3N_4, AT and CxAT (x = 0.7, 0.5, 0.3) composites.

with the oxygen adsorbed on the catalyst surface to generate more $\bullet O_2^-$ as the primary free radicals. The photoinduced holes will react with H_2O to produce $\bullet OH$. These reactive species can effectively photodegrade the acetaldehyde molecules on the catalyst surface into smaller organic molecules and finally become H_2O and CO_2. During the PCO process, the heterostructure is formed to improve the charge transfer efficiency. Either the Ag nanoparticles are deposited between TiO_2 and g-C_3N_4, which act as a conduction bridge to enable the electrons to carry out the directional transfer, or the direct contact between TiO_2 and g-C_3N_4 results in the formation of heterostructure, which can transfer photogenerated electrons directionally. Both of these conditions will facilitate the separation of photoinduced charges. As a result, the PCO performance of CAT nanocomposite is enhanced.
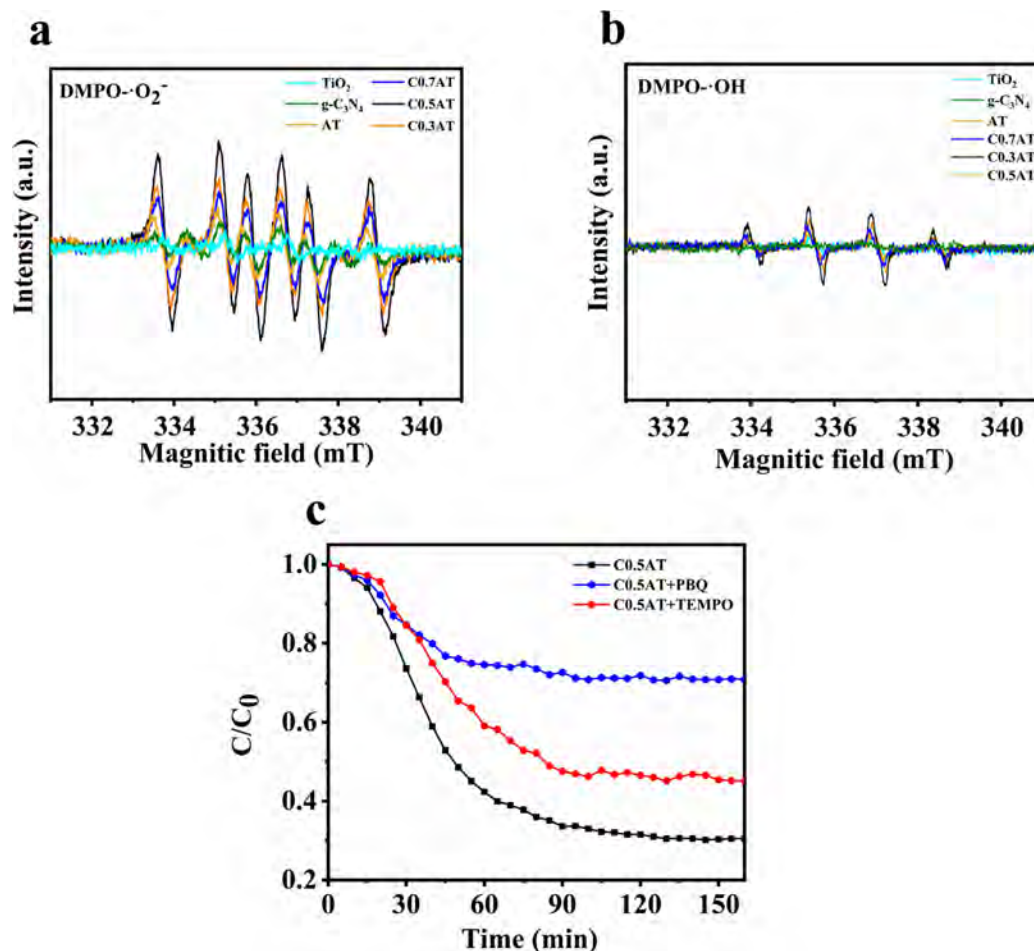
Fig. 9. ESR profiles for (a) superoxide radical ($\bullet O_2^-$) and (b) hydroxyl radical ($\bullet OH$) produced by TiO_2, g-C_3N_4, AT and CxAT (x = 0.7, 0.5, 0.3) composites, and (c) photoreaction for gaseous acetaldehyde of C0.5AT composite added with $\bullet O_2^-$ and $\bullet OH$ quenching agent under visible light condition (Repeat experiments for 3 times).
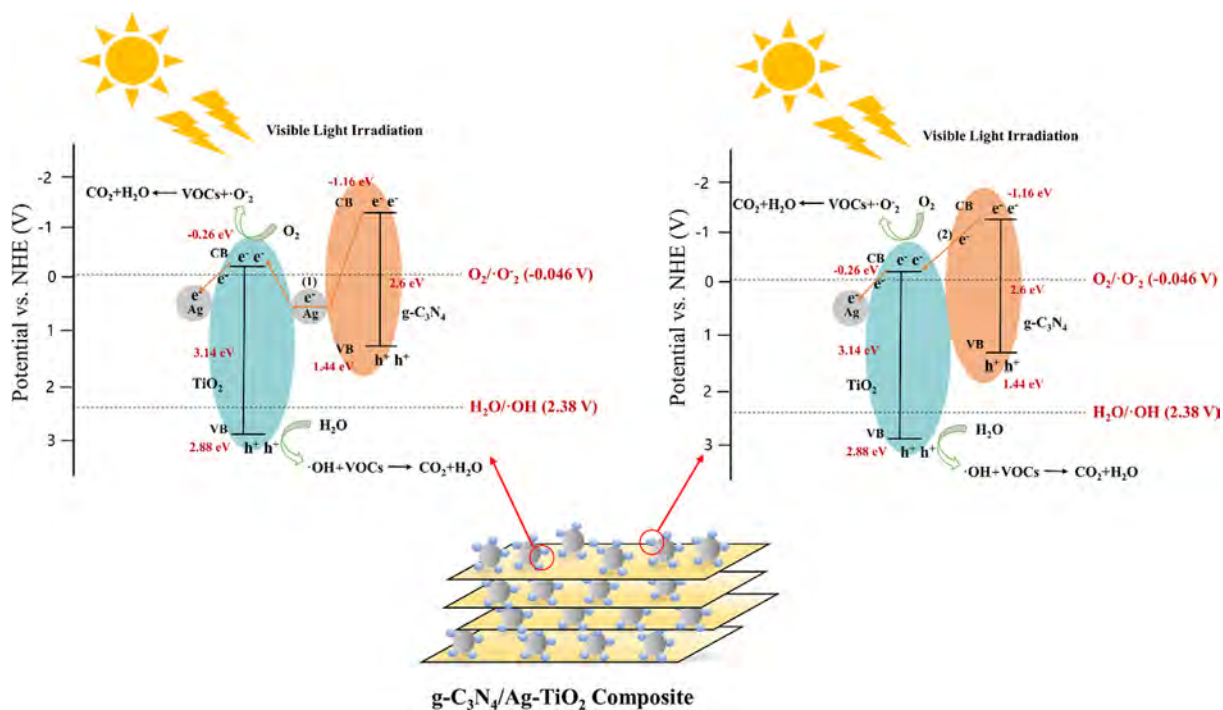

Fig. 10. Schematic of photodegradation towards VOCs over the CAT composite photocatalyst.

4. Conclusion

In summary, a ternary g-C$_3$N$_4$/Ag-TiO$_2$ photocatalyst has been synthesized by combining g-C$_3$N$_4$ and Ag-TiO$_2$ (AT) prepared by a chemical reduction method. The morphology, optical, and photocatalytic oxidation (PCO) performance of prepared photocatalysts were studied in detail. The results showed that ternary photocatalyst framework, incorporating AT with g-C$_3$N$_4$ significantly improved the PCO performance for the gaseous acetaldehyde photodegradation under visible light. These enhancements were associated with the synergistic effect of the strengthened adsorbability, better optical absorption and enhanced charge separation. Moreover, g-C$_3$N$_4$/50 wt% Ag-TiO$_2$ (C0.5AT) composite kept outstanding PCO performance after continuous irradiation and cyclic experiments, which indicated that the synthesized nanocomposites are stable for practical use. The kinetic study highlighted that the vital role of water in the PCO reaction of gaseous acetaldehyde. The electron spin-resonance (ESR) test and scavenger experiments proved that the photoinduced $\bullet O_2^-$ was the primary active radical for the gaseous acetaldehyde oxidation. This work provides significant achievement in developing ternary photocatalyst systems, which exhibits remarkable efficiency, durability, and potential for the visible light photocatalytic oxidation technology of low-concentration VOCs in the indoor environment.

CRediT authorship contribution statement

Congyu Wang: Investigation, Formal analysis, Data curation, Writing - original draft. **Zepeng Rao:** Writing - review & editing, Validation. **Asad Mahmood:** Conceptualization, Software, Writing - review & editing. **Xiao Wang:** Methodology, Formal analysis. **Yan Wang:** Conceptualization, Methodology, Supervision. **Xiaofeng Xie:** Project administration, Funding acquisition. **Jing Sun:** Methodology, Writing - review & editing, Supervision, Funding acquisition.

Declaration of Competing Interest

The authors declare the following financial interests/personal relationships which may be considered as potential competing interests: We wish to confirm that there are no known conflicts of interest associated with this publication and there has been no significant financial support for this work that could have influenced its outcome. We confirm that the manuscript has been read and approved by all named authors and that there are no other persons who satisfied the criteria for authorship but are not listed. We further confirm that the order of authors listed in the manuscript has been approved by all of us. We confirm that we have given due consideration to the protection of intellectual property associated with this work and that there are no impediments to publication, including the timing of publication, with respect to intellectual property. In so doing we confirm that we have followed the regulations of our institutions concerning intellectual property. We understand that the Corresponding Author is the sole contact for the Editorial process (including Editorial Manager and direct communications with the office). She is responsible for communicating with the other authors about progress, submissions of revisions and final approval of proofs. We confirm that we have provided a current, correct email address which is accessible by the Corresponding Author and which has been configured to accept email from jingsun@-mail.sic.ac.cn. Signed by all authors as follows: Congyu Wang, Zepeng Rao, Asad Mahmood, Xiao Wang, Yan Wang, Xiaofeng Xie, Jing Sun, 2021.4.11

References

[1] T. Shi, Y. Hu, M. Liu, C. Li, C. Zhang, C. Liu, How Do Economic Growth, Urbanization, and Industrialization Affect Fine Particulate Matter Concentrations? An Assessment in Liaoning Province, China, Int. J. Environ. Res. Public Health 17 (2020).

[2] H. Dai, J. Zhu, H. Liao, J. Li, M. Liang, Y. Yang, X. Yue, Co-occurrence of ozone and PM2.5 pollution in the Yangtze River Delta over 2013–2019: Spatiotemporal distribution and meteorological conditions, Atmos. Res. (2020).

[3] Y. Boyjoo, H. Sun, J. Liu, V.K. Pareek, S. Wang, A review on photocatalysis for air treatment: From catalyst development to reactor design, Chem. Eng. J. 310 (2017) 537–559.

[4] A. Luengas, A. Barona, C. Hort, G. Gallastegui, V. Platel, A. Elias, A review of indoor air treatment technologies, Rev. Environ. Sci. Bio/Tech. 14 (2015) 499–522.

[5] X. Chen, S.S. Mao, Titanium Dioxide Nanomaterials: Synthesis, Properties, Modifications, and Applications, Chem. Rev. 107 (2007) 2891–2959.

[6] Z. Shayegan, C.-S. Lee, F. Haghighat, TiO$_2$ photocatalyst for removal of volatile organic compounds in gas phase – A review, Chem. Eng. J. 334 (2018) 2408–2439.

[7] X. Fang, G. Lu, A. Mahmood, Y. Wang, X. Wang, X. Xie, Z. Tang, J. Sun, A novel ternary mica-titania@rGO composite pearlescent pigment for the photocatalytic degradation of gaseous acetaldehyde, Chem. Eng. J. 396 (2020).

[8] W. Lin, X. Xie, X. Wang, Y. Wang, D. Segets, J. Sun, Efficient adsorption and sustainable degradation of gaseous acetaldehyde and o-xylene using rGO-TiO$_2$ photocatalyst, Chem. Eng. J. 349 (2018) 708–718.

[9] R. Daghrir, P. Drogui, D. Robert, Modified TiO$_2$ For Environmental Photocatalytic Applications: A Review, Ind. Eng. Chem. Res. 52 (2013) 3581–3599.

[10] Y. Hu, X. Xie, X. Wang, Y. Wang, Y. Zeng, D.Y.H. Pui, J. Sun, Visible-Light Upconversion Carbon Quantum Dots Decorated TiO$_2$ for the Photodegradation of Flowing Gaseous Acetaldehyde, Appl. Surf. Sci. 440 (2018) 266–274.

[11] M.N. Chong, B. Jin, C.W. Chow, C. Saint, Recent developments in photocatalytic water treatment technology: a review, Water Res. 44 (2010) 2997–3027.

[12] Z. Rao, X. Xie, X. Wang, A. Mahmood, S. Tong, M. Ge, J. Sun, Defect Chemistry of Er^{3+}-Doped TiO$_2$ and Its Photocatalytic Activity for the Degradation of Flowing Gas-Phase VOCs, J. Phy. Chem. C 123 (2019) 12321–12334.

[13] X. Shi, Y. Zhang, X. Liu, H. Jin, H. Lv, S. He, H. Hao, C. Li, A Mild in-Situ Method to Construct Fe-Doped Cauliflower-Like Rutile TiO$_2$ Photocatalysts for Degradation of Organic Dye in Wastewater, Catalysts 9 (2019).

[14] J. Zhang, J. Xi, Z. Ji, Mo + N Codoped TiO2 sheets with dominant 001 facets for enhancing visible-light photocatalytic activity, J. Mater. Chem. 22 (2012).

[15] Z.M. El-Bahy, A.A. Ismail, R.M. Mohamed, Enhancement of titania by doping rare earth for photodegradation of organic dye (Direct Blue), J. Hazard. Mater. 166 (2009) 138–143.

[16] G. Lu, X. Wang, Y. Wang, G. Shi, X. Xie, J. Sun, Anti-oxidative microstructure design of ultra-stable N-TiO$_2$ composite for the gaseous photodegradation reactions, Chem. Eng. J. (2020).

[17] S. Weon, J. Kim, W. Choi, Dual-components modified TiO$_2$ with Pt and fluoride as deactivation-resistant photocatalyst for the degradation of volatile organic compound, Appl. Catal. B 220 (2018) 1–8.

[18] M. Stylidi, Visible light-induced photocatalytic degradation of Acid Orange 7 in aqueous TiO$_2$ suspensions, Appl. Catal. B 47 (2004) 189–201.

[19] X.-J. Wang, W.-Y. Yang, F.-T. Li, Y.-B. Xue, R.-H. Liu, Y.-J. Hao, In Situ Microwave-Assisted Synthesis of Porous N-TiO$_2$/g-C$_3$N$_4$ Heterojunctions with Enhanced Visible-Light Photocatalytic Properties, Ind. Eng. Chem. Res. 52 (2013) 17140–17150.

[20] B. Qiu, M. Xing, J. Zhang, Mesoporous TiO$_2$ nanocrystals grown in situ on graphene aerogels for high photocatalysis and lithium-ion batteries, J. Am. Chem. Soc. 136 (2014) 5852–5855.

[21] H. Tang, Z. Xia, R. Chen, Q. Liu, T. Zhou, Oxygen doped g-C3N4 with nitrogen vacancy for enhanced photocatalytic hydrogen evolution, 15 (2020) 3456-3461.

[22] E. Vesali-Kermani, A. Habibi-Yangjeh, H. Diarmand-Khalilabad, S. Ghosh, Nitrogen photofixation ability of g-C$_3$N$_4$ nanosheets/Bi$_2$MoO$_6$ heterojunction photocatalyst under visible-light illumination, J. Colloid Interface Sci. 563 (2020) 81–91.

[23] S. Asadzadeh-Khaneghah, A. Habibi-Yangjeh, M.S. Asl, Z. Ahmadi, S. Ghosh, Synthesis of novel ternary g-C$_3$N$_4$/SiC/C-Dots photocatalysts and their visible-light-induced activities in removal of various contaminants, J. Photochem. Photobiol. a-Chem. 392 (2020).

[24] K. Sun, J. Shen, Q. Liu, H. Tang, M. Zhang, S. Zulfiqar, C. Lei, Synergistic effect of Co(II)-hole and Pt-electron cocatalysts for enhanced photocatalytic hydrogen evolution performance of P-doped g-C$_3$N$_4$, Chin. J. Catal. 41 (2020) 72–81.

[25] X. Yu, J. Xie, Q. Liu, H. Dong, Y. Li, The origin of enhanced photocatalytic activity in g-C$_3$N$_4$/TiO$_2$ heterostructure revealed by DFT calculations, J. Colloid Interface Sci. 593 (2021) 133–141.

[26] B. Zhang, X. Ma, J. Ma, Y. Zhou, G. Liu, D. Ma, Z. Deng, M. Luo, Y. Xin, Fabrication of rGO and g-C$_3$N$_4$ co-modified TiO$_2$ nanotube arrays photoelectrodes with enhanced photocatalytic performance, J. Colloid Interface Sci. 577 (2020) 75–85.

[27] Y. Sheng, Z. Wei, H. Miao, W. Yao, H. Li, Y. Zhu, Enhanced organic pollutant photodegradation via adsorption/photocatalysis synergy using a 3D g-C$_3$N$_4$/TiO$_2$ free-separation photocatalyst, Chem. Eng. J. 370 (2019) 287–294.

[28] J. Li, M. Zhang, Q. Li, J. Yang, Enhanced visible light activity on direct contact Z-scheme g-C$_3$N$_4$-TiO$_2$ photocatalyst, Appl. Surf. Sci. 391 (2017) 184–193.

[29] C. Li, Z. Lou, Y. Yang, Y. Wang, Y. Lu, Z. Ye, L. Zhu, Hollowsphere Nanoheterojunction of g-C$_3$N$_4$@TiO$_2$ with High Visible Light Photocatalytic Property, Langmuir 35 (2019) 779–786.

[30] Q. Zeng, X. Xie, X. Wang, Y. Wang, G. Lu, D.Y.H. Pui, J. Sun, Enhanced photocatalytic performance of Ag@TiO$_2$ for the gaseous acetaldehyde photodegradation under fluorescent lamp, Chem. Eng. J. 341 (2018) 83–92.

[31] M. Stucchi, C.L. Bianchi, C. Argirusis, V. Pifferi, B. Neppolian, G. Cerrato, D.C. Boffito, Ultrasound assisted synthesis of Ag-decorated TiO$_2$ active in visible light, Ultrason. Sonochem. 40 (2018) 282–288.

[32] M. Logar, B. Jancar, S. Sturm, D. Suvorov, Weak polyion multilayer-assisted in situ synthesis as a route toward a plasmonic Ag/TiO$_2$ photocatalyst, Langmuir 26 (2010) 12215–12224.

[33] M. Klein, I. Nadolna, A. Gołąbiewska, P. Mazierski, T. Klimczuk, H. Remita, A. Zaleska-Medynska, The effect of metal cluster deposition route on structure and photocatalytic activity of mono- and bimetallic nanoparticles supported on TiO$_2$ by radiolytic method, Appl. Surf. Sci. 378 (2016) 37–48.

[34] J. Feng, D. Zhang, H. Zhou, M. Pi, X. Wang, S. Chen, Coupling P Nanostructures with P-Doped g-C$_3$N$_4$ As Efficient Visible Light Photocatalysts for H$_2$ Evolution and RhB Degradation, ACS Sus. Chem. Eng. 6 (2018) 6342–6349.

[35] H.-T. Ren, S.-Y. Jia, J.-J. Zou, S.-H. Wu, X. Han, A facile preparation of Ag$_2$O/P25 photocatalyst for selective reduction of nitrate, Appl. Catal. B 176–177 (2015) 53–61.

[36] G. Sui, J. Li, L. Du, Y. Zhuang, Y. Zhang, Y. Zou, B. Li, Preparation and characterization of g-C$_3$N$_4$/Ag–TiO$_2$ ternary hollowsphere nanoheterojunction catalyst with high visible light photocatalytic performance, J. Alloy. Compd. 823 (2020).

[37] H.M. Sung-Suh, J.R. Choi, H.J. Hah, S.M. Koo, Y.C. Bae, Comparison of Ag deposition effects on the photocatalytic activity of nanoparticulate TiO$_2$ under visible and UV light irradiation, J. Photochem. Photobiol., A 163 (2004) 37–44.

[38] N. Boonprakob, N. Wetchakun, S. Phanichphant, D. Waxler, P. Sherrell, A. Nattestad, J. Chen, B. Inceesungvorn, Enhanced visible-light photocatalytic activity of g-C$_3$N$_4$/TiO$_2$ films, J. Colloid Interface Sci. 417 (2014) 402–409.

[39] J. Yu, S. Wang, J. Low, W. Xiao, Enhanced photocatalytic performance of direct Z-scheme g-C$_3$N$_4$-TiO$_2$ photocatalysts for the decomposition of formaldehyde in air, PCCP 15 (2013) 16883–16890.

[40] J. Zhang, M. Zhang, G. Zhang, X. Wang, Synthesis of Carbon Nitride Semiconductors in Sulfur Flux for Water Photoredox Catalysis, ACS Catal. 2 (2012) 940–948.

[41] Y. Tan, Z. Shu, J. Zhou, T. Li, W. Wang, Z. Zhao, One-step synthesis of nanostructured g-C$_3$N$_4$/TiO$_2$ composite for highly enhanced visible-light photocatalytic H$_2$ evolution, Appl. Catal. B 230 (2018) 260–268.

[42] X. Fang, G. Lu, A. Mahmood, Z. Tang, Z. Liu, L. Zhang, Y. Wang, J. Sun, A novel ternary Mica/TiO$_2$/Fe$_2$O$_3$ composite pearlescent pigment for the photocatalytic degradation of acetaldehyde, J. Photochem. Photobiol. A 400 (2020).

[43] X.C. Zhang, J.A. Wang, W.Y. Hu, K.F. Zhang, B.J. Sun, G.H. Tian, B.J. Jiang, K. Pan, W. Zhou, Facile strategy to fabricate uniform black TiO$_2$ Nanothorns/ Graphene/Black TiO$_2$ Nanothorns Sandwichlike Nanosheets for Excellent Solar-Driven Photocatalytic Performance, Chem. Cat. Chem. 8 (2016) 3240–3246.

[44] Y. Yang, X. Li, C. Lu, W. Huang, G-C$_3$N$_4$ Nanosheets Coupled with TiO$_2$ Nanosheets as 2D/2D Heterojunction Photocatalysts Toward High Photocatalytic Activity for Hydrogen Production, Catal. Lett. 149 (2019) 2930–2939.

[45] L. Sun, J. Li, C.L. Wang, S.F. Li, Y.K. Lai, H.B. Chen, C.J. Lin, Ultrasound aided photochemical synthesis of Ag loaded TiO$_2$ nanotube arrays to enhance photocatalytic activity, J. Hazard. Mater. 171 (2009) 1045–1050.

[46] H. Liang, Z. Jia, H. Zhang, X. Wang, J. Wang, Photocatalysis oxidation activity regulation of Ag/TiO$_2$ composites evaluated by the selective oxidation of Rhodamine B, Appl. Surf. Sci. 422 (2017) 1–10.

[47] J.G. Yu, J.F. Xiong, B. Cheng, S.W. Liu, Fabrication and characterization of Ag-TiO$_2$ multiphase nanocomposite thin films with enhanced photocatalytic activity, App. Catal. B-Environ. 60 (2005) 211–221.

[48] Z.W. Tong, D. Yang, Y.Y. Sun, Z.Y. Jiang, Biomimetic synthesis of C$_3$N$_4$/TiO$_2$/Ag nanosheet composites with high visible-light photocatalytic performance, RSC Adv. 5 (2015) 56913–56921.

[49] S. Melchers, J. Schneider, A.V. Emeline, D.W. Bahnemann, Effect of H$_2$O and O$_2$ on the Adsorption and Degradation of Acetaldehyde on Anatase Surfaces-An In Situ ATR-FTIR Study, Catalysts 8 (2018).

[50] B. Tryba, P. Rychtowski, A. Markowska-Szczupak, J. Przepiorski, Photocatalytic Decomposition of Acetaldehyde on Different TiO$_2$-Based Materials: A Review, Catalysts 10 (2020).

[51] I. Papailias, N. Todorova, T. Giannakopoulou, D. Dvoranová, V. Brezová, D. Dimotikali, C. Trapalis, Selective removal of organic and inorganic air pollutants by adjusting the g-C$_3$N$_4$/TiO$_2$ ratio, Catal. Today (2019).

[52] T. Iihoshi, T. Ohwaki, J.J.M. Vequizo, A. Yamakata, Improvement of photocatalytic activity under visible-light irradiation by heterojunction of Cu ion loaded WO$_3$ and Cu ion loaded N-TiO$_2$, Appl. Catal. B 248 (2019) 249–254.

[53] S. Saqlain, B.J. Cha, S.Y. Kim, T.K. Ahn, C. Park, J.-M. Oh, E.C. Jeong, H.O. Seo, Y.D. Kim, Visible light-responsive Fe-loaded TiO$_2$ photocatalysts for total oxidation of acetaldehyde: Fundamental studies towards large-scale production and applications, Appl. Surf. Sci. 505 (2020).

[54] J. Zhang, Y. Hu, J. Qin, Z. Yang, M. Fu, TiO$_2$-UiO-66-NH$_2$ nanocomposites as efficient photocatalysts for the oxidation of VOCs, Chem. Eng. J. 385 (2020).

[55] E. Du, Y.X. Zhang, L. Zheng, Photocatalytic degradation of dimethyl phthalate in aqueous TiO$_2$ suspension: a modified Langmuir-Hinshelwood model, React Kinet Catal L 97 (2009) 83–90.

[56] F.V.S. Lopes, S.M. Miranda, R.A.R. Monteiro, S.D.S. Martins, A.M.T. Silva, J.L. Faria, R.A.R. Boaventura, V.J.P. Vilar, Perchloroethylene gas-phase degradation over titania-coated transparent monoliths, Appl. Catal. B-Environ. 140 (2013) 444–456.

[57] A. Mahmood, X. Wang, X. Xie, J. Sun, Degradation behavior of mixed and isolated aromatic ring containing VOCs: Langmuir-Hinshelwood kinetics, photodegradation, in-situ FTIR and DFT studies, J. Environ. Chem. Eng. 9 (2021) 105069.

[58] V. Chevalier, J. Martin, D. Peralta, A. Roussey, F. Tardif, Performance of HKUST-1 Metal-Organic Framework for a VOCs mixture adsorption at realistic concentrations ranging from 0.5 to 2.5 ppmv under different humidity conditions, Journal of Environmental, Chem. Eng. 7 (2019) 103131.

[59] A.H. Mamaghani, F. Haghighat, C.-S. Lee, Photocatalytic degradation of VOCs on various commercial titanium dioxides: Impact of operating parameters on removal efficiency and by-products generation, Build. Environ. 138 (2018) 275–282.

[60] N. Quici, M.L. Vera, H. Choi, G.L. Puma, D.D. Dionysiou, M.I. Litter, H. Destaillats, Effect of key parameters on the photocatalytic oxidation of toluene at low concentrations in air under 254+185 nm UV irradiation, Appl. Catal. B-Environ. 95 (2010) 312–319.

[61] A.H. Mamaghani, F. Haghighat, C.-S. Lee, Gas phase adsorption of volatile organic compounds onto titanium dioxide photocatalysts, Chem. Eng. J. 337 (2018) 60–73.

[62] A. Vittadini, A. Selloni, F.P. Rotzinger, M. Gratzel, Structure and energetics of water adsorbed at TiO$_2$ anatase (101) and (001) surfaces, Phys. Rev. Lett. 81 (1998) 2954–2957.

[63] L. Ge, C. Han, Synthesis of MWNTs/g-C$_3$N$_4$ composite photocatalysts with efficient visible light photocatalytic hydrogen evolution activity, Appl. Catal. B 117–118 (2012) 268–274.

[64] L.L. Lu, R. Shan, Y.Y. Shi, S.X. Wang, H.R. Yuan, A novel TiO$_2$/biochar composite catalysts for photocatalytic degradation of methyl orange, Chemosphere 222 (2019) 391–398.

[65] J. Li, K. Li, B. Lei, M. Ran, Y. Sun, Y. Zhang, K.-H. Kim, F. Dong, High-efficiency photocatalytic decomposition of toluene over defective InOOH: Promotive role of oxygen vacancies in ring opening process, Chem. Eng. J. (2020).

[66] Y.F. Chen, W.X. Huang, D.L. He, S.T. Yue, H. Huang, Construction of Heterostructured g-C$_3$N$_4$/Ag/TiO$_2$ Microspheres with Enhanced Photocatalysis Performance under Visible-Light Irradiation, ACS Appl. Mater. Interfaces 6 (2014) 14405–14414.

[67] K. Kočí, K. Matějů, L. Obalová, S. Krejčíková, Z. Lacný, D. Plachá, L. Čapek, A. Hospodková, O. Šolcová, Effect of silver doping on the TiO$_2$ for photocatalytic reduction of CO$_2$, Appl. Catal. B 96 (2010) 239–244.